DIAL Measurements of Free-Tropospheric Ozone Profiles in Huntsville, AL

Shi Kuang[1*], John Burris[2], Michael J. Newchurch[1], and Steve Johnson[3]

[1]*University of Alabama in Huntsville, 320 Sparkman Dr., Huntsville, Alabama 35805, USA*

[2]*NASA-Goddard Space Flight Center, Code 694, Greenbelt, Maryland 20771, USA*

[3]*NASA-Mashall Space Flight Center, Office Code VP61, Huntsville, Alabama 35812, USA*

Corresponding author: kuang@nsstc.uah.edu

ABSTRACT: A tropospheric ozone DIfferential Absorption Lidar (DIAL) system, developed jointly by NASA and the University of Alabama at Huntsville (UAH), measures free-tropospheric ozone profiles between 4-10 km. Located at 192 meters altitude in the Regional Atmospheric Profiling Laboratory for Discovery (RAPCD) on the UAH campus in Huntsville, AL, USA, this tropospheric ozone lidar operates under both daytime and nighttime conditions. Frequent coincident ozonesonde flights and theoretical calculations provide evidence to indicate the retrieval accuracy ranges from better than 8% at 4km to 40%-60% at 10 km with 750-m vertical resolution and 30-minute integration. With anticipated improvements to allow retrievals at both higher and lower altitudes, this ozone lidar, along with co-located aerosol and Doppler Wind Lidars, will provide a unique dataset for investigations of PBL and free-tropospheric chemical and dynamic processes.

1. Introduction

Measuring ozone variability at high spatial and temporal resolution increases our understanding of the Planetary Boundary Layer (PBL), PBL and free tropospheric exchange, stratosphere and troposphere exchange (STE), and the impact of lightning NOx on tropospheric ozone (*1*). Ozone, a triatomic oxygen molecule, is a key trace-gas species in the lower atmosphere. Within the troposphere, ozone is partially derived from transport processes that move ozone from the stratosphere into the troposphere and by the

25   oxidation of hydrocarbons originating from anthropogenic activity (*2*). Ozone's impact within the

26   free-troposphere, which extends from the top of the PBL to a maximum altitude that varies between 9-16km

27   depending on season and location, is more complex. Ozone is a powerful oxidant, and is harmful to both

28   plant and animal life; it is a strong greenhouse gas and an important component of photochemical smog.

29   However, it is also a key component of the atmospheric oxidizing cycle that cleans the air of harmful

30   pollutants.

31   Several techniques currently exist for making range-resolved measurements of tropospheric ozone.

32   The most common is the electrochemical concentration cell (ECC), which is attached to a balloon; ECCs

33   have been used since the 1960's to monitor ozone. These ozonesondes can profile ozone with a 100m

34   spatial resolution from the surface to 35km altitude with the accuracy of 5-10% (*3, 4*). Ozonesondes are

35   attractive because of their low upfront cost and their well-characterized behavior. They are, however, not

36   suitable for making continuous measurements because of cost and logistical considerations. Interesting

37   atmospheric phenomena that vary over periods less than one day are particularly difficult to monitor using

38   balloon sondes. Satellite observations can be used to derive total column ozone (*5*), stratospheric ozone

39   (*6-11*), and to extend measurements to altitudes that are inaccessible to ozonesondes (*12*). More recently,

40   high quality satellite observations of tropospheric ozone are becoming available (*4, 11, 13-18*). Although

41   the satellite measurements can produce global maps of ozone, their current measurement uncertainties (*19,*

42   *20*) along with their coarse spatial and temporal resolution limit their ability to observe short-term variations

43   of ozone. These techniques can be supplemented by lidar when a requirement exists for ozone retrievals

44   with high temporal (from 1 min to several hours) and spatial resolution (from tens of meters to 2 km) over

45   long periods. The DIAL technique minimizes the interference originating from aerosols and absorbing

46   species such as SO_2, and eliminates the need for obtaining an absolute calibration of the instrument. DIAL

47   has been successfully used to measure ozone within the planetary boundary layer (*21*), the free-troposphere

48   (*22-27*), and the stratosphere (*28-31*) for several decades. DIAL is evolving from ground-based and

49   airborne systems to systems suitable for long-term deployment in space (*32*). The technique derives ozone

50   concentrations by analyzing how rapidly the backscattered signals at two separate but closely spaced

51   wavelengths, one strongly absorbed by ozone and the other less strongly absorbed, fall off with altitude.

52   This measurement does not require that the absolute signal intensities are known but only how the two

53   signals change relative to one another with respect to altitude. The wavelengths are chosen to minimize

54   differential extinction due to aerosols, SO_2, and other species. The on-line to off-line signal ratio removes

55   the requirement that system parameters such as mirror size, pulse energy, and detection efficiency must be

56   known. Using electronically gated detection permits range-resolved measurements to a resolution as small

57   as ~15 m over acquisition times of several minutes. Although the up-front costs associated with a DIAL

58   system are considerably higher than a balloon ozonesonde operation, a DIAL system can acquire profiles

59   continuously under both daytime and nighttime conditions. The spatial and temporal resolution of a DIAL

60   lidar is more than sufficient to characterize short-term ozone variations for the photochemical studies of

61   vertical processes.

62   Several other research groups have employed ozone DIAL systems in both ground-based

63   configurations (*21, 24, 26, 31*) and aircraft configuration (*33, 34*) over the last two decades. The only

64   tropospheric ozone lidar in regular operation within the United States is located at the Jet Propulsion

65   Laboratory's Table Mountain facility northeast of Los Angeles in the San Gabriel Mountains (*35*). This

66   system Raman shifts 266 nm radiation to generate the on and offline wavelengths (289 and 299 nm). A lidar

67   system previously located on Fritz Peak in Colorado was operated for several years by Proffitt and Langford

68   (*26*). Like the McDermid system, the Proffitt lidar was located at relatively high altitude (~2300 m) to

69   maximize its altitude range and minimize interference from the boundary layer aerosols. Kempfer operated

70   a system in Germany using the output of a Raman shifted KrF excimer; this system was located at ~700 m

71   ASL (*36*). The location of the RAPCD ozone DIAL in the southeastern United States provides a unique

72   observational site within an interesting scientific area to study trace gas transport at the mid-latitudes (*37*).

73   Its low altitude facilitates the study of ozone within both polluted PBL and stratosphere-troposphere

74   exchange.

2. System Description

Housed in the RAPCD, the tropospheric ozone DIAL system is located on the UAH campus within the Huntsville city limits at an elevation of 196 m ASL and is currently designed for operation within the free-troposphere at altitudes between 4 and 10 km with a 150m vertical resolution. This approach permits the determination of ozone number densities under both daytime and nighttime conditions at high precision. Because of UAH's location, heavy aerosol pollution sometimes arises from sources such as forests, agriculture, and a number of large, coal fired, power plants. Compared with the clean free-troposphere, these aerosols require a larger dynamic range for detection system because of larger optical depth. Moreover, the rapid change of aerosols (e.g. due to convective activity) increases the measurement uncertainty for DIAL in the PBL and lower troposphere. Aside from aerosols, other differences between stratospheric and tropospheric systems arise from the much larger dynamic range in signal strength observed on tropospheric systems due to the signal's dependence on the $1/R^2$ term. The lower ozone number densities observed in the troposphere require higher absorption per unit length to achieve the same sensitivity as seen with stratospheric lidar systems. These differences have resulted in the Huntsville system being configured somewhat differently from instruments designed to measure stratospheric ozone or those that, while designed for tropospheric measurements, have been located at relatively high altitudes.

2.1 Wavelength selection

The optimum laser wavelengths result from the following four considerations: 1) The maximum measurable altitude determines the shortest wavelength; 2) The ability to reduce solar radiation in daytime operation determines the longest wavelength; 3) Minimizing the aerosol interference; 4) Avoiding SO_2 interference helps select among potential wavelength pairs. The DIAL wavelength selection is variable and can be optimized for the local ozone distribution, the absorption arising from non-ozone species, the measurement range and the specific system configuration including the output power, telescope mirror size and the photomultiplier's (PMT's) dynamic range. The optimum ozone DIAL wavelength selection has been explored by Megie (*38*) and further discussed by Proffitt (*26*) for tropospheric systems. We investigate

100 four specific criteria by model simulation under typically atmospheric conditions to select the optimum

101 wavelength pair.

102   While large cross sections are desirable for measurement sensitivity, they cause enhanced signal

103 attenuation due to both ozone absorption and Rayleigh extinction which limits the maximum altitude of the

104 measurement and increases the signal acquisition time. Fig. 1 shows the 2005 mean ozone profile over

105 Huntsville which is derived from the weekly ozonesonde measurements. The Huntsville ozone station at

106 UAH routinely launches balloon ozonesondes weekly at 19:00 UTC on Saturday. The ozonesondes

107 measure ozone up to 35 km with a 100m vertical resolution and 5-10% precision (*39*). These parameters are

108 listed in Table 1. Fig. 2 presents the modeled signal returns from 270 to 300 nm with the configuration of

109 a laser of 4 mJ/pulse, a telescope with 40 cm diameter, a PMT of 20% quantum efficiency, 5% totally

110 optical transmission efficiency, 1976 U.S. standard atmosphere, the ozone profile in Fig.1, and a fall-winter

111 rural aerosol model (*40*). The aerosol extinction profile was extrapolated to the 285-291 nm wavelength

112 from original 550 nm assuming that the Angstrom exponent is equal 1.1 (*41*), which is an approximate value

113 for rural-urban mixing aerosols. The dynamic range required for wavelengths below 270 nm to measure

114 ozone between 4 and 10 km reaches or exceeds the maximum value of our PMT ($\sim 10^5$). The spring and

115 summer tropospheric ozone concentrations in Huntsville are usually greater than the yearly average.

116 Therefore, the potential on-line wavelength must be greater than 270 nm. Also, the wavelengths from 270

117 to 280 nm cannot provide sufficient signal-to-background ratio at 10 km due to the overloading limitation

118 of our PMT. The background mainly consists of PMT dark counts and sky-light background. Dark counts

119 are a function of the voltage and temperature of PMT (*42*) and are observed as about 200 photon/s for our

120 experimental configuration. The comparison between modeled signals and background, as a function of

121 wavelength, is shown in Fig. 3. The modeled signal is calculated using the same characteristics as Fig. 2.

122 The expected sky background is simulated by NCAR TUV program (*43*) with the configuration in Table 1.

123 The modeling indicates that the potential on-line wavelength pair for our configuration should be larger

124 than 280 nm so that the detected signal is 1 order larger than the summation of sky background and dark

125 counts. To measure both wavelength channels by the same PMT and simplify the system design, we use a
126 broad band-pass filter (Barr Associates, 286.4/11nm), whose transmission as a function of wavelength is
127 shown by Fig. 4., to block the solar radiation. For a broadband band-pass filter the integrated sky
128 background over the filter bandwidth plus the dark counts actually determine the background for both
129 off-line and on-line wavelengths. The signal of the wavelengths below 285 is not large enough above 10 km
130 compared with the sum of sky background and dark counts to provide a useful measurement under mostly
131 atmospheric conditions. Increasing the laser power or removing neutral density filters could raise the
132 signal-to-background ratio at 10 km; however, this will lead to overloading of the PMTs at the near range.

133 The off-line wavelength is chosen at 291 because of both sky-background and interfering gases
134 considerations. The sky-background sharply increases in daytime with longer wavelength because of the
135 larger solar radiation even with an appropriate band-pass filter. As shown in Fig. 3, the signal at 291 nm is
136 about 2 orders of magnitude larger than sky background at 10 km. Fig. 5 [following Proffitt, *et al.*, 1997]
137 gives the signal-to-background ratio after passing through the band-pass filter. This model simulation
138 shows that the signal-to-background ratios are about 15 and 70 at 10 km for 285 and 291 respectively under
139 typical atmospheric condition, large enough to provide useful retrievals up to ~10 km.

140 Although retrieval errors due to aerosol interference are still of some concern in the PBL, they are
141 much less a concern in the free-troposphere. These errors can be explored by model simulation. Fig. 6
142 shows the modeled DIAL retrieval errors due to aerosol differential backscattering and extinction using the
143 parameters in Table 1 with a 750 m vertical resolution. The 285-291 pair will have a retrieval error at 4km
144 of less than 1% arising from uncorrected aerosol differential backscattering and extinction under typically
145 rural aerosol condition. If the aerosol loading is ten times higher, the error due to aerosol at 4 km increases
146 to 5%. These model simulations suggest that the errors due to aerosol above 4 km under both normal and
147 haze conditions are small relative to the statistical uncertainty which will be shown in later sections. The
148 error due to uncorrected Rayleigh extinction can be estimated with either the local sonde data or an
149 atmospheric model based on local climatology within the accuracy of 1% and will not be discussed here

150 further. Errors due to aerosol are extremely difficult to correct without additional local measurements

151 because of their large variability. These errors are sensitive to the wavelength pair and will increase with the

152 heavier aerosol loading. An approximate correction for aerosol has been given by Browell in 1985; at this

153 time, we make no aerosol correction in the free tropospheric lidar retrievals.

154 Constraining the daytime wavelengths below 292 nm requires that the impact of SO_2 is carefully

155 considered because its cross sections are comparable to those of ozone. The differential cross section of

156 SO_2 for 285-291 pair is $-4.8 \times 10^{-20} cm^2$ at 295 K (*44*). The error due to SO_2 is about -0.01% by assuming

157 that the SO_2 mixing ratio is 160 pptv under North America clean continental condition (*45*) and 60ppbv

158 ozone. This error could be up to -0.1% in a polluted air when SO_2 concentration reaches 1500 pptv.

159 However, its impact on our tropospheric measurements is negligible because it is much smaller than other

160 errors. Therefore, after fully considering the dynamic range of the PMTs, the measurement range, the

161 signal-to-background ratio, and the interfering species, we chose 285-291 wavelength pair for our lidar

162 system.

163 2.2 Hardware components

164 All DIAL systems consist of three major components: the transmitter, receiver, and detection

165 subsystems. The Huntsville transmitter consists of two identical dye lasers pumped by separate Nd:YAG

166 lasers. The characteristics of the DIAL system are listed in Table 2. Each pump laser has a fundamental

167 wavelength of 1064 nm, electro-optically Q-switched at 20 Hz using a plate polarizer, quarter waveplate,

168 and pockels cell. Each pulse is 5-7 ns Full Width at Half Maximum (FWHM) with a line-width of 1.0 cm^{-1}

169 and ~300 mJ of optical power. The output of each pump laser is frequency doubled by angle tuned

170 Potassium Dihydrogen Phosphate (KDP) crystals. The fundamental and frequency doubled pulses (532 nm)

171 are separated using dichroic mirrors (separators) where the fundamental is transmitted and absorbed by a

172 beam dump. The 532 nm pulses are reflected and redirected for use as a pump source for each tunable,

173 pulsed, dye laser as shown in Fig. 7. The dye lasers are software controlled with external computer systems

174 that select the user defined wavelength by rotating a reflection grating used to select a wavelength to be

175 amplified in the master oscillator. The dyes used as the gain medium are Rhodamine (R) 590 and 610.

176 R590 is used to produce 570 nm output and a combination of both R590 and R610 is used to produce 582nm

177 output. The output of each dye laser is frequency doubled using a Beta Barium Borate (BBO) crystal to

178 produce pulses with energies of 3-5 mJ at 285 and 291nm and a divergence less than 1mrad. The

179 divergences of both laser beams have been checked using a knife edge method (46). UV mirror

180 configuration separates the UV pulses from their visible fundamentals while redirecting the UV pulses to

181 a turning mirror which is aligned to reflect the pulses vertically into the atmosphere. Each laser pulse is

182 externally triggered by a function generator #1 such that there is a 25 ms temporal separation between the

183 firing of alternate pulses.

184   The receiver is a Newtonian telescope with a 40 cm primary and a two-channel aft optics unit as shown

185 in Fig. 8. Its current location is in the RAPCD lidar laboratory (lat:34.7250, lon:-86.6450) where it views

186 the atmosphere through a roof hatch with a 1m by 1m opening. A series of selectable apertures permit the

187 telescope's field of view (FOV) to be changed as part of the alignment process. Provision exists to insert

188 both band-pass and neutral density filters into the optical path to restrict the solar background and/or

189 attenuate a channel's signal in the event that the returns are too high. The current band-pass filters have a

190 transmission of 35% at 285 nm and $<10^{-8}$ beyond 300 nm as shown in Fig. 4. The system currently operates

191 with two altitude channels. The signal is split, so the high-altitude channel receives ~90% of the light, and

192 the low-altitude channel receives ~10%. This division effectively restricts the lower-altitude channel to no

193 higher that ~4 km; the high-altitude channel routinely covers 4-10 km and on occasion has reached 12 km.

194   The low-altitude system will be discussed in a separate paper. With the FOV of the receiver set at 1.5 mrad

195 for normal operation, 0.9 m separation distance between the laser beam and the telescope axis, and 1mrad

196 divergence of the laser beams, full overlap occurs at about 3 km. Larger FOVs lower the altitude at which

197 full overlap between the laser and telescope occur but significantly increase background noise arising from

198 the sun and city sky light.

199   RAPCD's detection system currently utilizes photon counting to facilitate operations at the maximum

200 achievable altitude. Two EMI 9813 QA PMTs, which have been used extensively for many years on a

201 number of Goddard Space Flight Center lidar systems, are used – one for each channel. The outgoing laser

202 pulse of each laser is detected by a photodiode (PD) laser-pulse detector, which sends the trigger to the

203 function generator #2. One channel of the function generator outputs a pulse to trigger a pulse generator that

204 controls the clock and bin width pulses for the return signal; the other channel sends a delayed pulse to gate

205 the PMT. The range bin width is set at 1 μs corresponding to an effective vertical resolution of 150 m. The

206 timing of the whole system including the laser trigger, gate signal, range bin width, clock, and ground bin

207 can be checked by an LED test (47) in which LED light simulates the backscattered return, and all signals

208 are monitored by an oscilloscope. The signal recording of the MCS board is supposed to start the same time

209 as the PD detection of laser-pulse trigger for our setting. But a small offset between them has been observed

210 during our LED test. This offset will be corrected before the retrieval. It is necessary to gate the high altitude

211 channel off for approximately the first 15 μs to maintain the PMT's linearity and minimize the impact of

212 signal-induced bias (SIB) on the background count rate. The signal from the output of the PMT is processed

213 by a 300 MHz discriminator to minimize noise counts and stored in one of four multichannel scalar (MCS)

214 boards (Tennelec/nucleus MCS-II) – one board for each channel (285High, 285Low, 291High and

215 291Low). Data files are stored in a small microcomputer and processed immediately after acquisition

216 ceases.

217 **3. Data processing**

218 3.1 Raw data processing

219 Before ozone can be retrieved, several operations, designed to improve the measurement precision, are

220 carried out. First, multiple laser shots are averaged to increase the signal-to-noise ratio (SNR). The RAPCD

221 DIAL currently uses data acquired over a 30-minute interval for each retrieval. The second step involves

222 accounting for dead time. At high counting rates (~10 MHz for the RAPCD lidar), a second signal pulse

223 arriving at the discriminator before it has recovered from the previous pulse may not be counted – a period

224 know as dead time. This time has been experimentally determined to be ~9 ns for the RAPCD lidar using

225 calibrated neutral density filters to characterize the system's response to accurately known count rates. A

226 simple relationship, Eq. (1)., between the actual and measured count rates allows the impact of dead time

227 on the data to be removed. Eq. (1). can be solved numerically for the actual count rate, r, using the measured

228 count rate, R and the experimentally determined dead-time T_d.

229 $$R = re^{-rT_d} \qquad\qquad (1)$$

230 Third, background counts due to PMT dark counts and the sky background are removed. These counts

231 are constant and are derived using data bins for which there are no signal returns. The averaged value is

232 then subtracted off all data channels. The final step involves smoothing the counts to reduce random noise.

233 Our configuration currently employs a 5-point (750 m) moving average that is applied to returns from all

234 altitudes; smoothing reduces the effectively vertical resolution to 750 m. After initial processing, a

235 correction is applied to remove SIB from the data. This bias, also called signal-induced noise (SIN),

236 appears as a slowly decaying, weak, noise source superimposed on the normal returns and becomes an issue

237 if the PMT is exposed to an extremely intense light pulse (48). SIB can persist for several hundred

238 microseconds and has a strong impact on data from the lidar's upper range where signal and noise counts

239 become comparable. With uncorrected SIB, the raw signal fall off more slowly at higher altitudes resulting

240 in lower retrieved ozone values. It is system specific and characterized under various operational

241 conditions. For RAPCD, SIB has more influence on the shorter wavelength channel which falls off more

242 rapidly with altitude. Unless a mechanical shutter is employed to physically block the optical path to the

243 PMT and thereby eliminate SIB, its behavior must be characterized using a model. Cairo and Zhao have

244 successfully used a double exponential function for this purpose (48, 49). However, this correction

245 increases measurement uncertainties because both the scaling and exponential lifetimes are difficult to

246 determine without additional independent measurements. A more practical technique is to employ a single

247 exponential fit to the residual background (25, 26, 50). For the high altitude channels of the RAPCD lidar,

248 the function's coefficients are empirically determined using a single exponential fit to data acquired ~110

249 to ~160 µs after data acquisition starts. The start and length of the exponential fit could vary with different

250   channels (either wavelength channels or altitude channels), atmospheric structures, and lidar configurations

251   because these parameters impact the intensity of the detected signal. Future improvement to the RAPCD

252   DIAL includes an optical chopper to remove the SIB and all need for SIB correction.

253   3.2 Dial retrieval

254   The DIAL retrieval algorithm takes advantage of the reduction of uncertainty resulting from aerosols

255   and non-ozone absorption gases using the differential technique. The retrieval using a single wavelength

256   becomes unreliable when aerosols and non-ozone absorption gases are present; however, conditions often

257   exist where both single wavelength and DIAL retrievals produce comparable results. Excellent discussions

258   concerning the DIAL technique can be found in the book by Measures [1984] and papers by Browell [1985]

259   and Godin [1999]; a brief discussion of the technique is also provided in Appendix I.

260   Vertical ozone profiles can also be retrieved using a single wavelength retrieval (*51*). When sonde density

261   profiles are available, this technique serves as an independent check on the DIAL retrievals and can provide

262   useful information about the impact of aerosols on the measurement.

263   **4. Performance**

264   4.1 Raw data performance

265   Figure 9 (a) and (c) displays a daytime example of raw photon counts with deadtime and background

266   corrections along with a comparison to counts expected from a model calculation. The lidar data were taken

267   at 13:22 local time, Sep. 16, 2006, and the balloon ozonesonde measurement with a 100-m resolution was

268   made at 13:16 the same day. A ±10% uncertainty in the ozonesonde measurement is represented by gray

269   envelope. The ozonesonde also provides the atmospheric profiles for single wavelength retrieval, the

270   temperature correction for ozone absorption cross section and Rayleigh correction in Dial retrieval. The raw

271   lidar data are integrated over 36000 shots (30 min). The background including the sky light and dark counts

272   is estimated about 1.4×10^{-2} counts/us/shot at far range for either wavelength. The PMT is gated at 3 km (20

273   µs). The peak counts at ~3km of both 285 and 291 are ~2.8 photons/us/shot, which gives the peak

274 signal-to-background ratio about 200. The signal-to-background ratio of either 285 or 291 at 10 km is less

275 than the model calculation in Fig. 5 in part due to high ozone concentration in the lower troposphere.

276 Though a higher signal-to-background ratio is desired, increasing the signal strength (e.g., by increasing the

277 output energy or removing ND) will further distort the far range signal by SIB. The dead-time correction,

278 background subtraction, moving averaging, and SIB correction are applied on the raw data as described in

279 previous section. The final ozone profile is smoothed using a running average over 750m range cell. The

280 averaging upon raw data and retrieved ozone profile reduce the vertical range resolution to 750m from

281 original 150m bin width.

282 4.2 Retrieved ozone profile

283 In Fig. 9 (b) and (d) the corrected data shows good agreement with the model between 4 and 10 km.

284 Notice some intermittent thin clouds between 11 and 12 km. Although the 291nm laser penetrates the small

285 cloud, too few of the 285 photons survive the cloud to retrieve a useful signal. In Fig. 9 (e), the 30-min lidar

286 retrievals agree with sonde within an accuracy of 20% at all altitudes. The error bars show the 1-sigma

287 statistical uncertainty of the DIAL retrieval over a 30-min interval. The error bars indicate that the DIAL

288 measurement precision increases from 5% at 4 km to ~50% at 10 km. Fig. 9(e) indicates good consistency

289 between the single wavelength retrievals at both wavelengths and the DIAL retrieval between 4 and 10 km.

290 **5. Error Analysis**

291 According to the sources, we can divide the errors in DIAL measurements into four categories: 1).

292 Statistical uncertainties, ε_1, due to atmospheric turbulence effects, signal, and background noise fluctuations;

293 2). Error, ε_2, due to differential backscattering and extinction of non-ozone gases (O_2, SO_2, NO_2, etc.) and

294 aerosols; 3). Error, ε_3, due to ozone absorption cross section; and 4). Error, ε_4, related to instruments and

295 electronics. ε_1 is a random error; ε_2, ε_2, and ε_3 are systematical errors.

296 5.1 Statistical error

297 With the assumption of a Poisson distribution governing photon counting, ε_1 can be written as:

298
$$\varepsilon_1 = \frac{1}{2O_3(R+1/2\Delta R)\Delta R\Delta\sigma_{O3}} \sqrt{\frac{1}{P_{on}(R)} + \frac{1}{P_{on}(R+\Delta R)} + \frac{1}{P_{off}(R)} + \frac{1}{P_{off}(R+\Delta R)}} \quad (2)$$

299 It is easy to show that ε_1 is proportional to $(\Delta R^3 NAP_L)^{-1/2}$, where N is the shots of integration and A is the

300 area of the telescope and P_L is the emitted laser power. ε_1 also depends on the weather condition and

301 vertical ozone structure. For 750 m vertical resolution and 36000-shot integration, generally ε_1 is <5% at

302 4 km and 40%-60% at 10 km in our DIAL retrievals.

303 5.2 Interference by non-ozone species

304 ε_2 includes the interference from O_2, SO_2, NO_2, and aerosols. The O_2 interference should be

305 considered as one of the error sources in the DIAL retrieval (52) because the quantity of O_2 is large in the

306 atmosphere. The O_2 absorption spectrum below 300 nm is composed of the Herzberg band system and the

307 O_2-O_2 and O_2-X collision-induced absorption bands (53). The accurate calculation of the O_2 interference is

308 difficult because the oxygen dimmer absorption theory has not been entirely established (54), and the

309 uncertainty of the O_2 cross section measurement is quite high. Based on the data set of the Fally group (53,

310 55, 56), the differential O_2 effective absorption cross section (57) is less than 4.5×10^{-27}, which results a

311 DIAL retrieval error <1.5% with a 60ppbv ozone mixing ratio. As discussed in a previous section, the

312 errors due to SO_2 are ~0.01% under clear conditions and ~0.1% under very polluted conditions. The NO_2

313 absorption cross sections at 285 and 291 are 7.07×10^{-20} and 9.32×10^{-20} cm^2 respectively at 293K with an

314 uncertainty of 3.2% (58). The NO_2 differential cross section is -2.25×10^{-20} cm^2 for the 285 and 291 pair.

315 NO_2 is highly variable and inhomogeneous over time and space. The mean NO_2 mixing ratios over Houston

316 and Nashville are recorded less than 0.2 ppbv above 800 hPa in the Texas Air Quality Study (TexAQS) and

317 Southern Oxidants Study (SOS) (59), leading to the DIAL retrieval error ~0.007% under the 60ppbv

318 constant ozone assumption. The HCHO absorption cross sections at 285 and 291 are 4.17×10^{-20} and

319 2.06×10^{-20} cm^2, respectively, at 293K (58) result in an HCHO differential cross section of 2.11×10^{-20} cm^2.

320 The local HCHO information is not available. The maximum HCHO mixing ratio at 600 hpa (~4.3 km)

321 recorded in Houston was 150 pptv during TexAQS and SOS campaign (*59*). This leads to a 0.015% error in

322 DIAL retrieval. The impact caused by differential Rayleigh extinction can be modeled within an accuracy

323 of 1% using balloon sonde retrievals of atmospheric density or by employing climatological models.

324   The main concern comes from the aerosol interference which depends on the wavelengths and

325 wavelength separation. Even though the aerosol optical properties could be retrieved from a third

326 wavelength, the differential effect for a DIAL wavelength pair still has some uncertainty. Within the PBL,

327 where the statistical errors are small, differential aerosol backscattering and extinction can be the dominant

328 error sources for a DIAL ozone retrieval (*22, 24, 25*). Our model simulation in Fig. 6(b) has shown the

329 DIAL retrieval errors due to aerosol could be up to 25% in PBL when aerosol loading is 10 times higher

330 than the average. In the free-troposphere, the aerosol concentration decreases very quickly and the

331 increasing statistical errors quickly dominate. The errors due to aerosols are smaller than 1% above 4 km

332 using fall-winter rural aerosol model.   If the aerosol values are increased by a factor of ten, the resulting

333 ozone uncertainties increase to 5% at 4 km.

334 5.3 Uncertainty in ozone absorption cross section

335   ε_3 The uncertainty of Bass-Paur ozone cross section is believed to be less than 2% (*54, 60, 61*). The

336 retrieval error due to ozone absorption cross section should be less than 3% even with the temperature

337 dependence considered.

338 5.4 Errors related to instruments and electronics

339   ε_4 could be caused by misalignment, imperfect dead-time, and SIB correction. The first aspect is

340 negligible when both lasers are well-aligned and reach the full overlap altitude. The latter two can be

341 investigated by an LED or null-profile test. The error caused by SIB usually is larger than dead-time since

342 the dead-time behavior can be easier characterized. The SIB can be estimated better by exponential fit with

343 longer integration. For the 36000-shot integration data, ε_4 is believed to be <1% at 4 km and <5% at 8 km.

344　The summary of the errors in RAPCD-DIAL measurement is given by Table 3 assuming 60 ppbv constant

345　ozone in troposphere for a 36000-shot integration data.

346　　An example of continuous lidar measurements is shown by Fig. 10. Ten 30-minute DIAL

347　measurements shown in Fig. 10 (a) were made between 11:00 and 17:00 local time on Dec. 23, 2006. Fig.

348　10 (b) shows the average Dial profile of the 10 retrievals and its 1-sigma standard deviation which

349　represents the measured uncertainty. The average ozone DIAL profile shows good agreement with

350　ozonesonde measurement between 4 and 10km. The standard deviation increases from ~5% at 4 km to

351　~60% at 10 km. This data set along with the ozonesonde measurements show that ε_1 is most significant in

352　all of the errors though the ozone variation could contribute a small part to the different between the DIAL

353　and ozonesonde.

354　**6. Future work**

355　6.1 Modifications to the high altitude channel

356　　The effectiveness of the current system's high-altitude channels is limited by the need to electronically

357　protect against the large backscattering signal originating from the first kilometer or so above the telescope.

358　 These large initial signals interfere with the PMT's linearity and make it difficult to properly characterize

359　the PMT's background count rate. The current system attempts to minimize these effects through a

360　combination of several techniques. The first technique restricts the backscattered signal by limiting the

361　maximum per pulse laser energy and by attenuating the signal before reaching the high channel through a

362　combination of optical splitters and neutral density filters. Both approaches reduce signal returns from

363　higher altitudes thereby limiting the maximum achievable altitude and/or increasing signal averaging time.

364　 An electronic gating circuit is employed that permits the gain of the PMT to be turned off for periods as

365　short as 10 microseconds. Although this does not protect the photocathode directly, it does prevent the

366　resulting photoelectrons from being amplified and causing both gain and background nonlinearity problems

367　in the future. This technique, however, provides only partial protection from the problems caused by the

368　large initial backscatter pulses. The final approach raises the altitude at which complete overlap between

369   the laser beam and telescope's FOV occurs. This technique reduces the initial backscatter pulse as seen by

370   the detector but occurs at the cost of signal from the lower end of the channel's range. We intend to resolve

371   these issues through the addition of a mechanical chopper. Choppers are routinely employed on lidar

372   systems to protect PMTs by physically blocking the optical path between the telescope and PMT. This

373   blocking prevents the large initial backscatter pulse from being seen by the PMT's photocathode. Shielding

374   the high channel's PMT from returns originating within the first couple of kilometers will permit higher, per

375   pulse, laser energies thus enabling faster data acquisition, higher maximum altitudes, and higher

376   measurement precision.

377   6.2 Modifications to the low-altitude channel

378   The current low-altitude channel is ineffective because the separation between laser beam and the

379   telescope (optimized for the high altitude channel) is too great for full overlap in the PBL. The integrated

380   modification will introduce a primary mirror with an effective diameter of 10 cm rather the 40 cm. The

381   smaller telescope will thus collect fewer photons from an altitude range that already sees extremely large

382   signals and will experience complete overlap at a much lower altitude than is currently the case. The current

383   PMTs, EMI 9813s, will be replaced by the much smaller Hamamatsu 7400s; this change will significantly

384   shrink the size of the instrument with no sacrifice to performance. These PMTs have already seen extensive

385   operational use on the NASA GSFC AROTEL lidar. Three separate splitters will allow a custom

386   determination of the optimum signal split between these channels. The detection electronics for the high

387   and low channels will be updated by replacing the current multi-channel scalar boards with state-of-the-art

388   detection modules having both simultaneous analog and photon counting capabilities.

389   To enhance the lidar's measurement capabilities within the boundary layer, a scanner will be added to

390   permit range resolved measurements of ozone from the surface to the top of the PBL in any direction. This

391   consideration will enable the study of pollution transport within the PBL at high resolution and permit the

392   study of ozone variability on spatial scales of hundreds of meters.

393   **7. Conclusion**

394 The RAPCD-DIAL system can measure ozone profiles between 4 and 10 km with an errors ranging from

395 <8% at 4k m to 40%~60% at 10 km. The error sources include the statistical uncertainty, differential

396 scattering and absorption from non-ozone species, uncertainty in ozone absorption cross section, and

397 imperfection of dead-time and SIB correction. The statistical uncertainty dominates the error sources and

398 could be reduced by increasing the sampling time or reducing the range resolution. The aerosol interference

399 in the free-troposphere is relatively small. A mechanical chopper will be added into our high-altitude

400 channel to improve signal linearity. A smaller telescope and detection modules will be used for our

401 low-altitude channel in the future to decrease the full overlap altitude and avoid PMT saturation in the near

402 range.

403 **8. Acknowledgements**

409

410 <div align="center">**Appendix**</div>

411 **A. Dial retrieval algorithm**

412 The average ozone number density above full overlap altitude between range R and $R + \Delta R$ is solved by:

413
$$[O_3](R + \frac{1}{2}\Delta R) =$$

414
$$\frac{1}{2\Delta R \Delta \sigma_{O3}} \ln[\frac{P_{on}(R)P_{off}(R+\Delta R)}{P_{off}(R)P_{on}(R+\Delta R)}] \qquad (A1a)$$

415
$$-\frac{1}{2\Delta R \Delta \sigma_{O3}} \ln[\frac{\beta_{off}(R)\beta_{on}(R+\Delta R)}{\beta_{on}(R)\beta_{off}(R+\Delta R)}] \qquad (A1b)$$

416
$$-\frac{1}{\Delta \sigma_{O3}}(\alpha_{on} - \alpha_{off}) \qquad (A1c)$$

417 where the subscript 'on' and 'off' represent the on-line and off-line wavelengths respectively; P is

418 detected power or photons; β is total backscatter coefficient; α is total extinction coefficient except for

419 ozone absorption; $\Delta\sigma_{O3}$ is differential ozone absorption cross section. P, β, and α are dependents of

420 R and wavelength. Strictly, $\Delta\sigma_{O3}$ is R dependent, as well, because it is the function of temperature which

421 varies with R. The DIAL equation reduces to only (A1a), signal term when the differential scattering and

422 extinction from non-ozone species are ignored. Term (A1b), differential backscattering term, consists of

423 Rayleigh (molecular) and Mie (aerosol) differential backscattering. Term (A1c), differential extinction term,

424 consists of differential Rayleigh extinction, aerosol extinction, and non-ozone gaseous absorption including

425 O_2, SO_2, NO_2 etc. Rayleigh effects usually can be corrected in practice with the assistance of a local

426 atmospheric sonding profile. The aerosol effects should be corrected when they are significant enough,

427 especially in PBL.

428 **B. Single wavelength retrieval algorithm**

429 The vertical ozone profile can be retrieved using the backscattered signal of one laser with the Rayleigh and

430   Mie backscattering and extinction known. The average ozone number density between R and $R + \Delta R$ is

431   solved by (*62*):

432 $$[O_3](R + \frac{1}{2}\Delta R) = \frac{1}{2\sigma_{O3}\Delta R} \times \{\ln[\frac{P_\lambda(R)}{P_\lambda(R + \Delta R)}] - \ln[\frac{\beta_\lambda(R)/R^2}{\beta_\lambda(R + \Delta R)/(R + \Delta R)^2}] - 2\alpha_\lambda(R)\Delta R\} \quad (B1)$$

433   Where λ is wavelength and σ_{O3} is absorption cross section of ozone. $\beta_\lambda(R)$ is the sum of Rayleigh and

434   Mie components. $\alpha_\lambda(R)$ is the sum of Rayleigh, Mie, and absorption gaseous components. $\beta_\lambda(R)$ and

435     $\alpha_\lambda(R)$ can be approximately reduced to only Rayleigh component in the unpolluted free-troposphere and

436   stratosphere. However, the retrieval with a single laser tends to be unreliable when aerosols and other

437   non-ozone absorption gases are heavily present. The single wavelength retrieval is also more sensitive to

438   the atmospheric density profile than DIAL retrieval. The errors of single wavelength retrieval are discussed

439   in another paper. Interested readers should refer to Measures' book. However, when simultaneous

440   atmospheric temperature and pressure profiles are available, it will be a good reference for our DIAL

441   retrieval in the free-troposphere where aerosols are much less of a concern than in the PBL.

442

443

444

REFERENCES

445

446 1. A. J. DeCaria, K. E. Pickering, G. L. Stenchikov, L. E. Ott, "Lightning-generated NOX and its
447   impact on tropospheric ozone production: A three-dimensional modeling study of a
448   Stratosphere-Troposphere Experiment: Radiation, Aerosols and Ozone (STERAO-A)
449   thunderstorm" *J. Geophys. Res.* **110** (2005).
450 2. J. Lelieveld, F. J. Dentener, "What controls tropospheric ozone?" *J. Geophys. Res.* **105**, 3531
451   (2000).
452 3. S. J. Oltmans *et al.*, "Summer and spring ozone profiles over the North Atlantic from ozonesonde
453   measurements" *J. Geophys. Res.* **101**, 29 (1996).
454 4. M. J. Newchurch, D. Sun, J. H. Kim, X. Liu, "Tropical Tropospheric Ozone Derived using
455   Clear-Cloudy Pairs (CCP) of TOMS Measurements" *J. of Atmos. Chem. Phys.* **3**, 683 (2003).
456 5. R. D. McPeters *et al.*, *Nimbus-7 Total Ozone Mapping Spectrometer (TOMS) Data Products User's
457   Guide*, NASA (Washington, D.C., 1996).
458 6. M. P. McCormick, J. M. Zawodny, R. E. Veiga, J. C. Larsen, P. H. Wang, "An overview of SAGE
459   I and II ozone measurements" *Planet Space Sci.* **37**, 1567 (1989).
460 7. D. M. Cunnold, L. Froidevaux, J. M. Russell, B. Connor, A. Roche, "Overview of UARS ozone
461   validation based primarily on intercomparisons among UARS and Stratospheric Aerosol and Gas
462   Experiment II measurements" *J. Geophys. Res.* **101**, 10 (1996).
463 8. J. M. Russell III *et al.*, "The Halogen Occultation Experiment" *J. Geophys. Res.* **98**, 10 (1993).
464 9. M. J. Newchurch, D. M. Cunnold, H. J. Wang, "Stratospheric Aerosol and Gas Experiment
465   II--Umkehr ozone profile comparisons" *J. Geophys. Res.* **100**, 14029 (1995).
466 10. M. J. Newchurch, D. M. Cunnold, J. Cao, "Intercomparison of Stratospheric Aerosol and Gas
467   Experiment (SAGE) with Umkehr[64] and Umkehr[92] ozone profiles and time series: 1979-1991"
468   *J. Geophys. Res.* **103**, 31 (1998).
469 11. J. P. Burrows *et al.*, "The Global Ozone Monitoring Experiment (GOME): Mission concept and
470   first scientific results" *J. Atmos. Sciences* **56**, 151 (1999).
471 12. R. D. McPeters, G. J. Labow, B. J. Johnson, "A satellite-derived ozone climatology for
472   balloonsonde estimation of total column ozone" *J. Geophys. Res.* **102**, 8875 (1997).
473 13. K. V. Chance, J. P. Burrows, D. Perner, W. Schneider, "Satellite measurments of atmospheric
474   ozone profiles, including tropospheric ozone, from ultraviolet/visible measurements in the nadir
475   geometry: a potential method to retrieve tropospheric ozone" *J. Quant. Spectrosc. Radiat. Transfer*
476   **57**, 467 (1997).
477 14. J. R. Ziemke, S. Chandra, P. K. Bhartia, "Two new methods for deriving tropospheric column
478   ozone from TOMS measurements: Assimilated UARS MLS/HALOE and convective-cloud
479   differential techniques" *J. Geophys. Res.* **103**, 22 (1998).
480 15. J. H. Kim, M. J. Newchurch, K. Han, "Distribution of Tropical Tropospheric Ozone determined by
481   the scan-angle method applied to TOMS measurements" *J. Atmos. Sci.* **58**, 2699 (2001).
482 16. J. H. Kim, S. Na, M. J. Newchurch, K.J. Ha, "Comparison of Scan-Angle Method and Convective
483   Cloud Differential Method in Retrieving Tropospheric Ozone from TOMS" *Environ. Mon. Assess.*
484   **92**, 25 (2004).
485 17. J. H. Kim, M. J. Newchurch, "Climatology and trends of tropospheric ozone over the eastern
486   Pacific Ocean: The influences of biomass burning and tropospheric dynamics" *Geophys. Res. Lett.*
487   **23**, 3723 (1996).
488 18. X. Liu *et al.*, "Ozone profile and tropospheric ozone retrievals from Global Ozone Monitoring
489   Experiment: Algorithm description and validation" *J. Geophys. Res.* **110** (2005).

490   19.   M. J. Newchurch, X. Liu, J. H. Kim, P. K. Bhartia, "On the accuracy of TOMS retrievals over
491   cloudy regions" *J. Geophys. Res.* **106**, 32 (2001).

492   20.   M. J. Newchurch, X. Liu, J. H. Kim, "Occurrence of Ozone Anomalies over Cloudy Areas in
493   TOMS Version-7 Level-2 Data" *J. Geophys. Res.* (2000).

494   21.   Y. Zhao, R. D. Marchbanks, R. M. Hardesty, paper presented at the 42nd SPIE Annual meeting,
495   Application of Lidar to Current Atmospheric Topics II, Proceedings of SPIE #3127 1997.

496   22.   E. V. Browell, S. Ismail, S. T. Shipley, "Ultraviolet DIAL measurements of O3 profiles in regions
497   of spatially inhomogeneous aerosols" *App. Opt.* **24**, 2827 (1985).

498   23.   G. Ancellet, A. Papayannis, J. Pelon, G. Mégie, "DIAL Tropospheric Ozone Measurement Using
499   a Nd:YAG Laser and the Raman Shifting Technique" *J. of Atmos. Ocean. Tech.* **6**, 832 (1989).

500   24.   A. Papayannis, G. Ancellet, J. Pelon, G. Mègie, "Multiwavelength lidar for ozone measurements in
501   the troposphere and the lower stratosphere" *App. Opt.* **29**, 467 (1990).

502   25.   J. A. Sunesson, A. Apituley, D.P.J.Swart, "Differential absorption lidar system for routine
503   monitoring of tropospheric ozone" *App. Opt.* **33**, 7045 (1994).

504   26.   M. H. Proffitt, A. O. Langford, "Ground-based differential absorption lidar system for day or night
505   measurements of ozone throughout the free-troposphere" *App. Opt.* **36**, 2568 (1997).

506   27.   T. Fukuchi, "Tropospheric O3 measurements by simultaneous differential absorption lidar and null
507   profiling" *Opt. Eng.* **40** (2001).

508   28.   J. Pelon, S. Godin, G. Megie, "Upper stratospheric (30-50 km) lidar observations of the ozone
509   vertical distribution" *J. Geophys. Res.* **91**, 8667 (1986).

510   29.   O. Uchino, I. Tabata, "Mobile lidar for simultaneous measurements of ozone, aerosols, and
511   temperature in the stratosphere" *App. Opt.* **30**, 2005 (1991).

512   30.   T. J. McGee, M. R. Gross, U. N. Singh, J. J. Butler, P. E. Kimvilakani, "Improved stratospheric
513   ozone lidar" *Opt. Eng.* **34**, 1421 (1995).

514   31.   I. S. McDermid, "Differential absorption lidar system for tropospheric and stratospheric ozone
515   measurements" *Opt. Eng.* **30** (1991).

516   32.   E. V. Browell, S. Ismail, W. B. Grant, "Differential absorption lidar(DIAL) measurements from air
517   and space" *App. Phys.*, 399 (1998).

518   33.   E. V. Browell *et al.*, "NASA multipurpose airborne DIAL system and measurements of ozone and
519   aerosol profiles" *App. Opt.* **22**, 522 (1983).

520   34.   T. J. McGee *et al.*, "The Airborne, Raman Ozone, Temperature and Aerosol Lidar (AROTAL):
521   Instrument and Measurements" *in prep.* (2007).

522   35.   S. McDermid, G. Beyerle, D. A. Haner, T. Leblanc, "Redesign and improved performance of the
523   tropospheric ozone lidar at the Jet Propulsion Laboratory Table Mountain Facility" *App. Opt.* **41**,
524   7550 (2002).

525   36.   U. Kempfer, W. Carnuth, R. Lotz, T. Trickl, "A weide-range ultraviolet lidar system for
526   tropospheric ozone measurements: Development and application" *Rev. Sci. Instrum.* **65**, 3145
527   (1994).

528   37.   O. R. Cooper *et al.*, "A springtime comparison of tropospheric ozone and transport pathways on the
529   east and west coasts of the United States" *J. Geophys. Res.* **110**, 21 (2005).

530   38.   G. J. Megie, G. Ancellet, J. Pelon, "Lidar measurements of ozone vertical profiles" *Appl. Opt.* **24**
531   (1985).

532   39.   M. J. Newchurch, M. A. Ayoub, S. Oltmans, B. Johnson, F. J. Schmidlin, "Vertical Distribution of
533   Ozone at Four Sites in the United States" *J. Geophys. Res.* **108(D1)**, 4031 (2003).

534   40.   A. S. Jursa, "Handbook of Geophysics and the Space Environment" (1985).

535   41.   T. F. Eck *et al.*, "Wavelength dependence of the optical depth of biomass burning, urban, and desert
536   dust aerosols" *J. Geophys. Res.* **104**, 31 (1999).

537   42.   A. G. Wright, "An Investigation of Photomultiplier Background" *J. Phys. E: Sci. Instrum.* **16**, 300
538   (1983).

539   43.   S. Madronich, S. Flocke, paper presented at the NATO ASI Series I: Global Environmental Chang,

540 Berlin 1997.

541 44. J. Rufus, G. Stark, P. L. Smith, J. C. Pickering, A. P. Thorne, "High-resolution photoabsorption
542   cross section measurements of SO2, 2: 220 to 325 nm at 295 K" *J. Geophys. Res.* **108** (2003).

543 45. J. H. Seinfeld, S. N. Pandis, *Atmospheric Chemistry and Physics, From Air Pollution to Climate
544   Change*, John Wiley & Sons (New York, 1998).

545 46. ISO, *Standard for the Measurement of Beam Widths, Beam Divergence, and Propagation Factors,
546   Proposal for a Working Draft* (1991).

547 47. S. Kuang, J. Burris, M. J. Newchurch, S. Johnson, "Diagnosis of Lidar systematic errors by LED
548   synthetic signal" *in prep* (2007).

549 48. F. Cairo, F. Congeduti, M. Poli, S. Centurioni, G. d. Donfrancesco, "A survey of the signal-induced
550   noise in photomultiplier detection of wide dynamics luminous signals" *Rev. Sci. Instrum.* **67**, 3274
551   (1996).

552 49. Y. Zhao, "Signal-induced fluorescence in photomultipliers in differential absorption lidar systems"
553   *Appl. Opt.,* **38** (1999).

554 50. T. J. McGee *et al.*, "Lidar measurements of stratospheric ozone during the STOIC campaign" *J.
555   Geophys. Res.* **100**, 9255 (1995).

556 51. O. Uchino, M. Maeda, M. Hirono, "Applications of Excimer lasers to Laser-Radar Observations of
557   the Upper Atmosphere" *IEEE J. Quantum Electron.* **QE-15** (1979).

558 52. R. Volkamer, T. Etzkorn, A. Geyer, U. Platt, "Correction of the oxygen interference with UV
559   spectroscopic (DOAS) measurements of monocyclic aromatic hydrocarbons in the atmosphere"
560   *Atmos. Enviro.* **32**, 3731 (1998).

561 53. S. Fally *et al.*, "Fourier Transform Spectroscopy of the O2 Herzberg bands. III. Absorption
562   cross-sections of the collision-induced bands and of the Herzberg continuum" *J. Mol. Spectrosc.*
563   **204**, 10 (2000).

564 54. J. Orphal, "A critical review of the absorption cross-sections of O3 and NO2 in the 240-790 nm
565   region" *J. Phtotoch. and Photobio. A.*, 185 (2003).

566 55. A. Jenouvrier *et al.*, "Fourier transform spectroscopy in the O2 Herzberg bands: I- Rotational
567   analysis" *J. Mol. Spectrosc.* **198**, 136 (1999).

568 56. M.-F. Mérienne *et al.*, "Fourier transform spectroscopy of the O2 Herzberg bands. II. Band
569   oscillator strengths and transition moments" *J. Mol. Spectrosc.* **202**, 171 (2000).

570 57. A. Amoruso, L. Crescentini, "Oxygen dimerization and pressure dependence of the absorption
571   cross-section in the Herzberg continuum" *J. Quant. Spect. Rad. Trans.* **53**, 457 (1995).

572 58. K. Bogumil *et al.*, "Measurements of molecular absorption spectra with the SCIAMACHY
573   pre-flight model: instrument characterization and reference data for atmospheric remote-sensing in
574   the 230–2380 nm region" *J. Photochem. Photobiol A: Chem* **157**, 167 (2003).

575 59. R. V. Martin *et al.*, "Evaluation of GOME satellite measurements of tropospheric NO 2 and HCHO
576   using regional data from aircraft campaigns in the southeastern United States" *J. Geophys. Res.* **109**
577   (2004).

578 60. A. M. Bass, R. J. Paur, "Absorption cross-sections for ozone: the temperature dependence" *J.
579   Photochem.* **17** (1981).

580 61. J. Orphal, K. Chance, "Ultraviolet and visible absorption cross-sections for HITRAN" *J. Quant.
581   Spectrosc. Radiat. Trans.* **82**, 491 (2003).

582 62. M. R. Measures, "Laser remote sensing: Fundamentals and applications" (1984).

583
584
585

586

587

Table 1. Parameters for model simulation

Laser energy	4 mJ/pulse
The diameter of telescope primary mirror	40 cm
Telescope field-of-view	1.5 mrad
Receiver bandwidth	1 nm
PMT quantum efficiency	20%
Total optical transmission efficiency	5%
Solar zenith angle	30°
Temperature and Pressure profiles	1976 US standard atmosphere
Ozone profile	mean profile over Huntsville in 2005
Aerosol profile	fall-winter rural aerosol model

588

589

590

591   Table 2. Characteristics of DIAL system

System	Specification
Transmitter	
Lasers	Continuum Nd:YAG, 20 Hz repetition rate, 5-7 ns pulse length, ~300 mJ/pulse at 1064 nm, 80 mJ/pulse at 532 nm
Dye	Rhodamine 590 and 610
Emitted energy	4-5 mJ/pulse at 285 nm, divergence<1 mrad 3-4 mJ/pulse at 291 nm, divergence<1 mrad
Receiver	
Telescope	Newtonian, 40.6 cm diameter, f/4.5, 1.5 mrad FOV
Filter	Barr band-pass filter (286.4/11nm) and neutral density filters
Detector	Electron Tubes 9813QA, ~28% quantum efficiency
Discriminator	Phillips Scientific 300 MHz
Signal Processing	Tennelec/nucleus MCS-II cards, 200 MHz, 24 bit

592

593

594   Table 3. Summary of the errors in RAPCD-DAIL measurements[*]

Errors		4 km	10 km
ε_1, statistical error		~5%	~40-60%
ε_2, interference by non-ozone species	Aerosol	~1% under clear condition; ~5% under haze condition	~1%
	SO$_2$	~-0.01% under normal condition ~-0.1% under polluted condition	
	NO$_2$	~-0.007%	
	O$_2$	~1.5%	
	HCHO	~0.015%	
	Rayleigh	~1% using local radiosonde profile	
ε_3, due to uncertainty in $\Delta\sigma_{O3}$		~3%	
ε_4, due to SIB and dead-time		~1%	~5%
Total error		~6.3%-~8.0%	~40.5%-~60.3%

595   * The errors are estimated by assuming 60 ppbv constant ozone in troposphere for 750 m vertical resolution

596   and 36000-shot integration data.

597

598

599

600

601
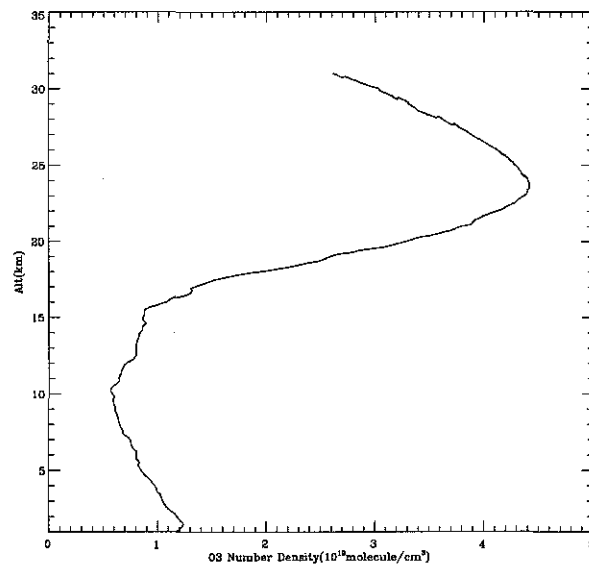
Fig. 1. Mean ozone profile over Huntsville (2005). Huntsville ozone station in UAH routinely launches balloon ozonesonde weekly at 19:00 UTC on Saturday. The ozonesondes measure ozone up to 35km with a 100 m vertical resolution and 5-10% accuracy.
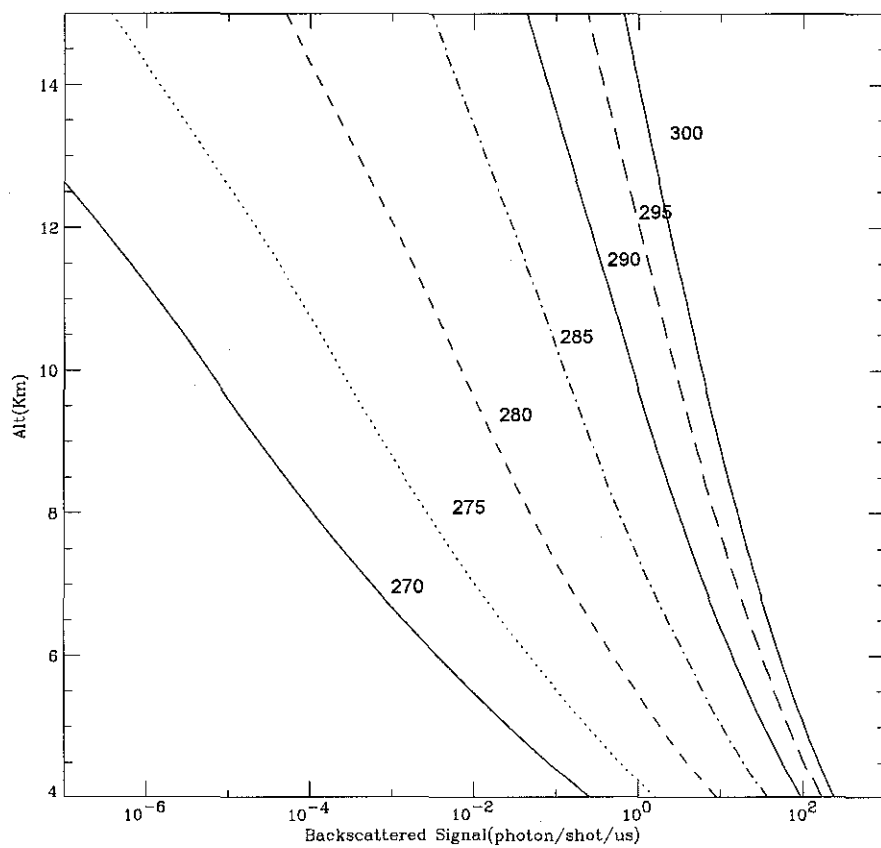
Fig. 2. Modeled lidar signal returns from 270 to 300 nm using the parameters in Table 1.
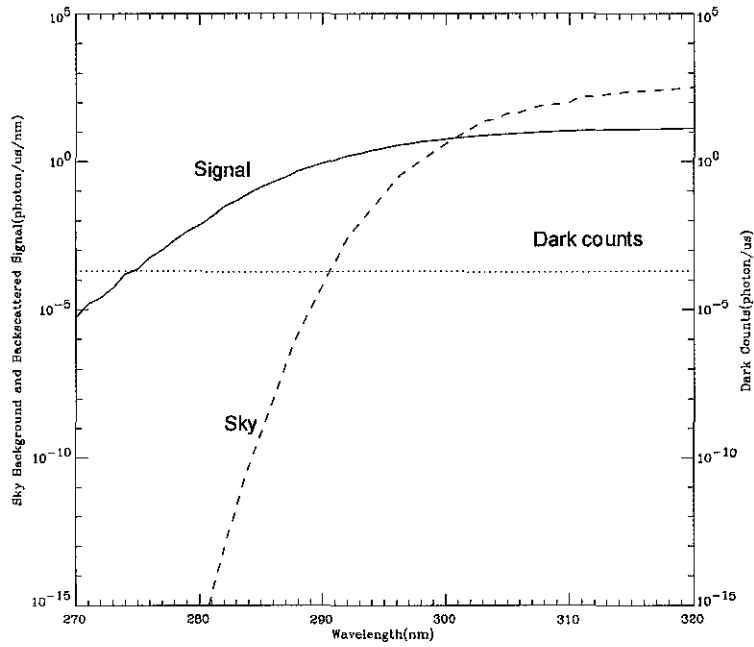
Fig. 3. Comparison of expected background including sky background and dark counts with modeled

signal return at 10km without band-pass filter. The signal return and sky background are simulated

with the parameters in Table 1.
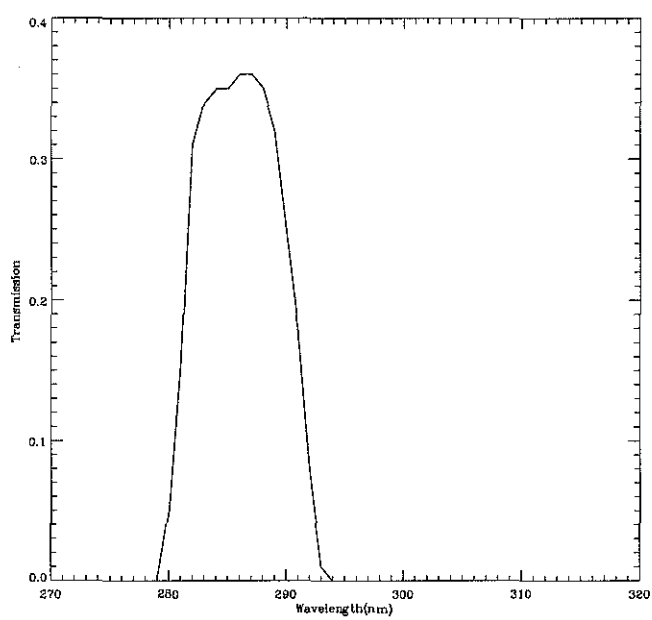
Fig. 4. Transmission of Barr filters (286.4/11nm) as a function of wavelength.
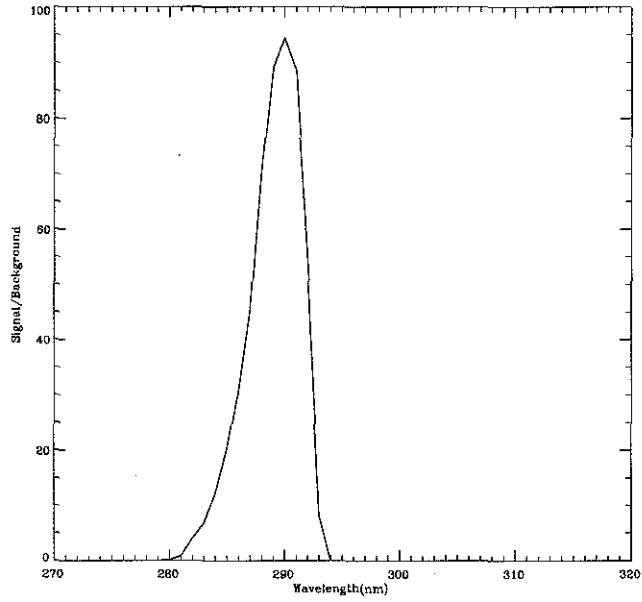
Fig. 5. Expected signal-to-background ratio at 10 km after passing through the band-pass filter as a function of wavelength. The signal return and sky background are modeled with the parameters in Table 1. The sky background is integrated over the transmission of band-pass filter in Fig. 4. The dark counts are assumed constant level at 200 photons/s.
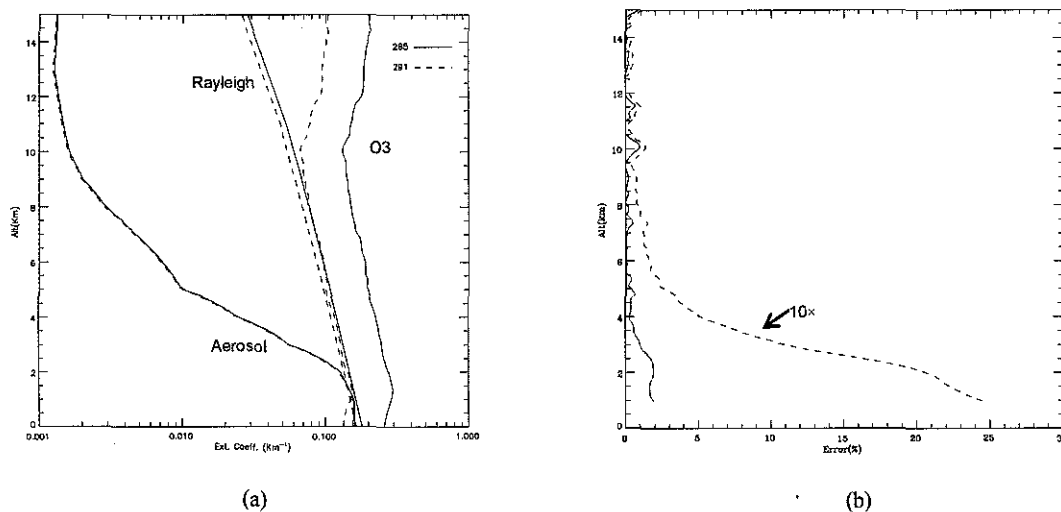
Fig. 6. Modeled DIAL retrieval errors due to aerosol. (a) Extinction as a function of altitude for aerosols (using the rural fall-winter aerosol profiles at 285 and 291 nm), Rayleigh scattering (using the 1976 US Standard Atmosphere) and ozone (using the 2005 Huntsville averaged ozone profile). (b) DIAL retrieval errors due to differential aerosol backscattering and extinction for 285-291 nm pair with a 750 m range resolution. The solid line represents the corresponding retrieval error of the aerosol model in (a). The dash line represents the retrieval error arising from an aerosol loading 10 times higher than given in the aerosol model in (a).
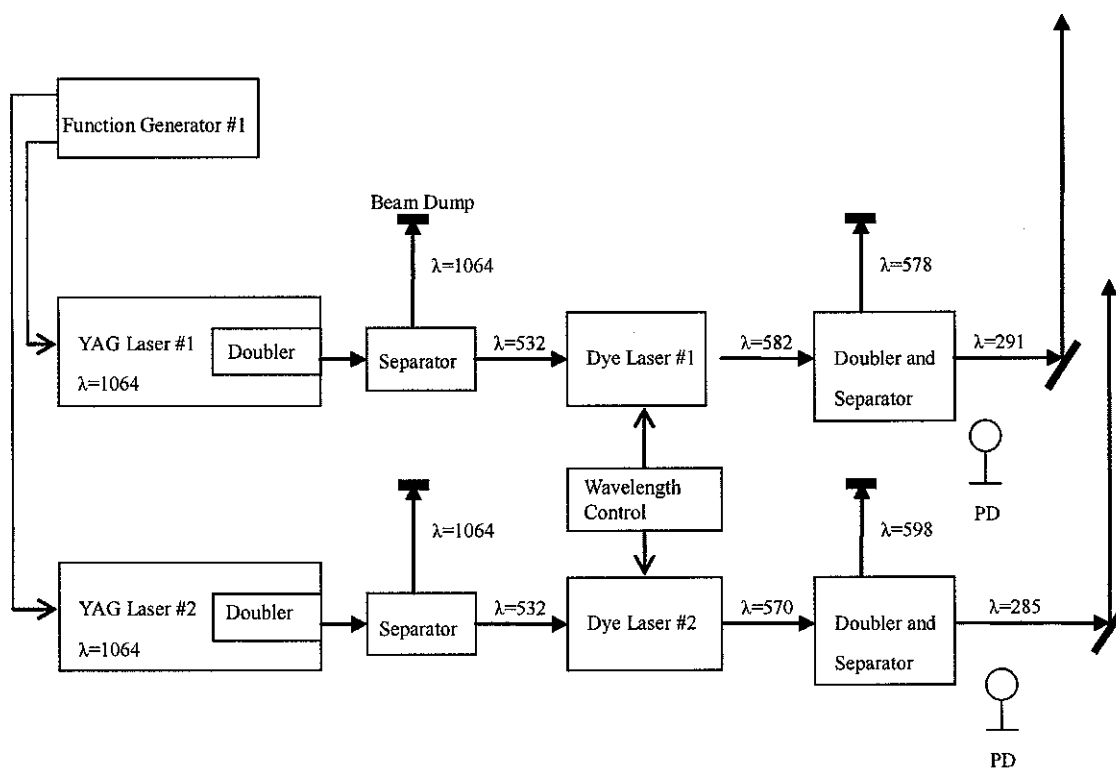
Fig. 7. Transmitter diagram.
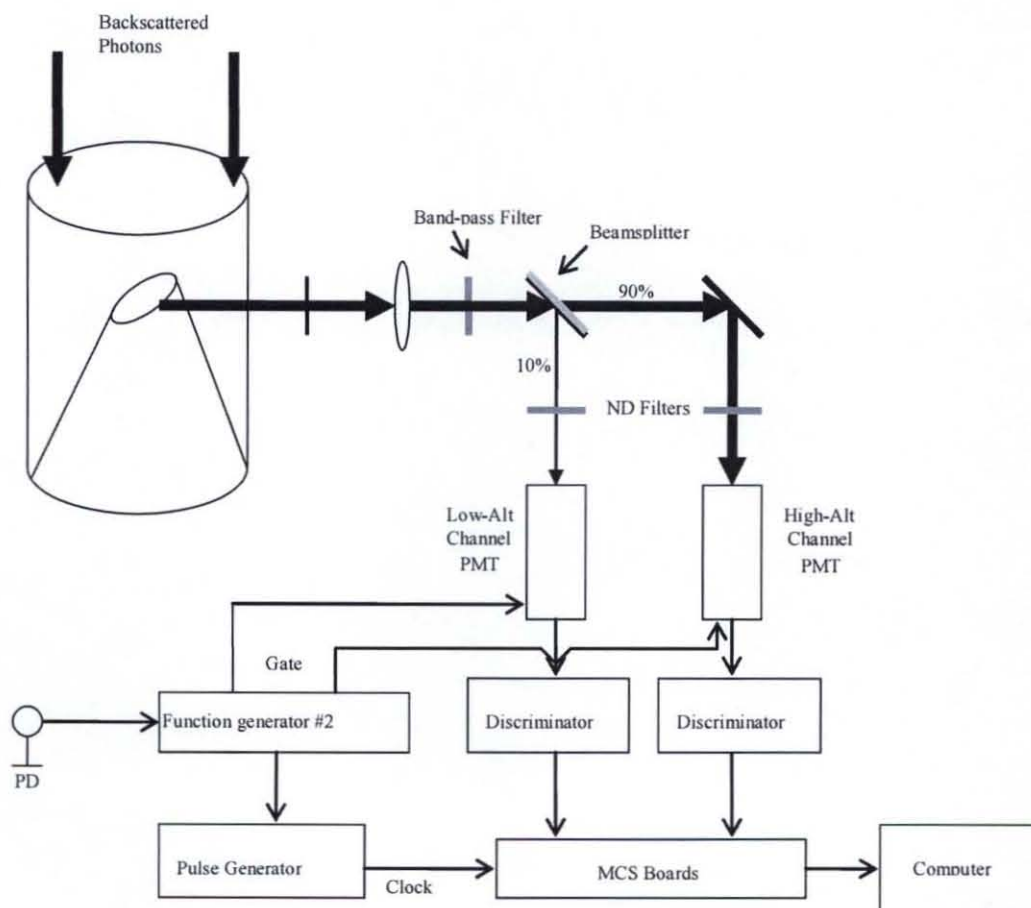
Fig. 8. Diagram of the receiver and detector.
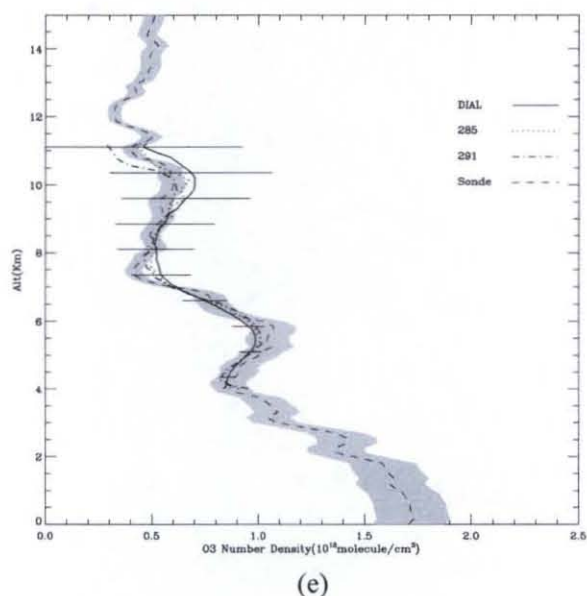
(a)

(b)

(c)

(d)

(e)
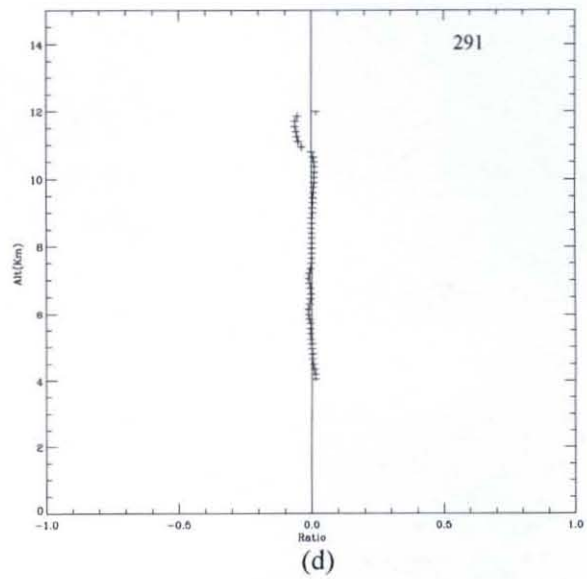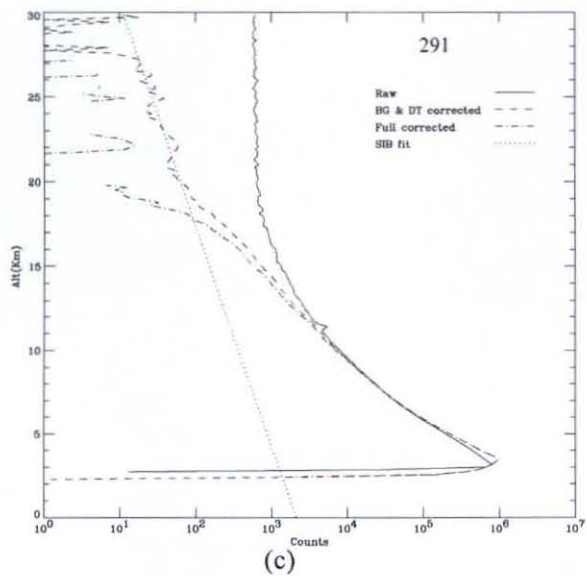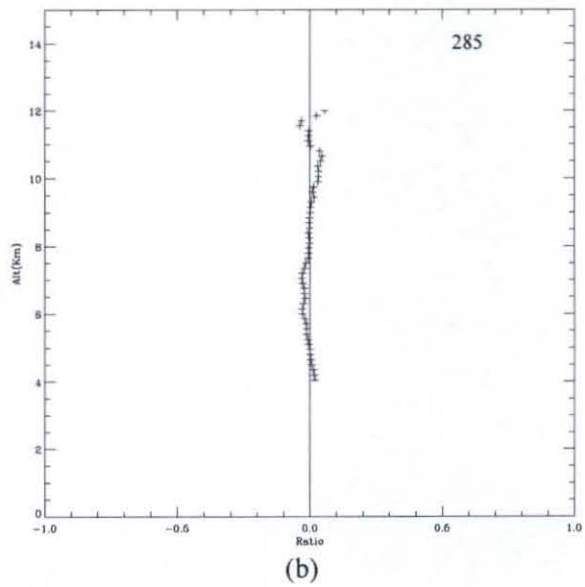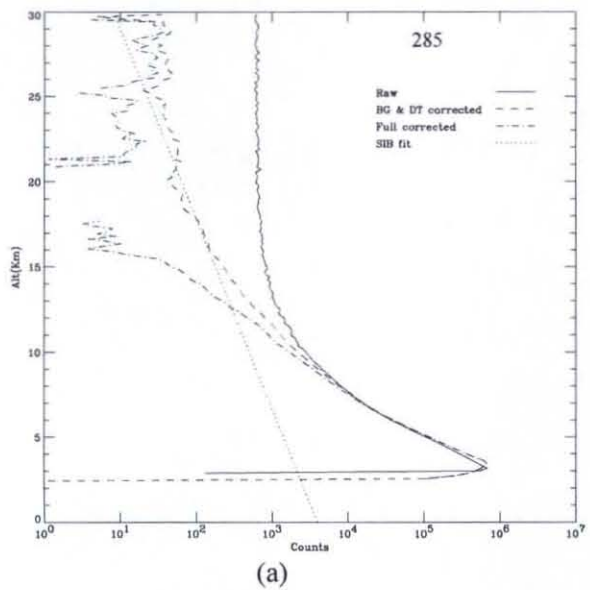
Fig. 9. DIAL daytime measurement at 13:22 local time, Sep. 16, 2006. (a) 285nm raw, background-and-dead-time (BG & DT) corrected, and fully corrected data. The raw data were integrated over 36000 shots, 30 min for 20Hz repetition frequency. (b) Difference, (model-data)/model, between 285 fully corrected data and model. (c) 291nm raw, dead-time-and-background corrected, and fully corrected data. (d) Difference, (model-data)/model, between 291 fully corrected data and model. (e) Comparison of ozonesonde measurement and DIAL and with single wavelength retrievals with 750 m vertical resolution. The balloon ozonesonde was launched at 13:16 local time and also provided the temperature and pressure profiles to calculate single wavelength retrieval, correct ozone absorption cross section and Rayleigh effects in Dial retrieval. The ±10% uncertainty of the ozonesonde is represented by gray envelope. The error bars represent the 1-sigma statistical uncertainty of Dial retrieval.
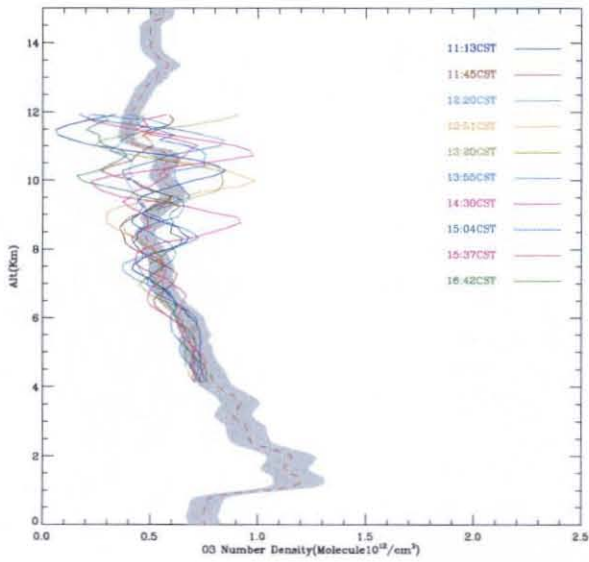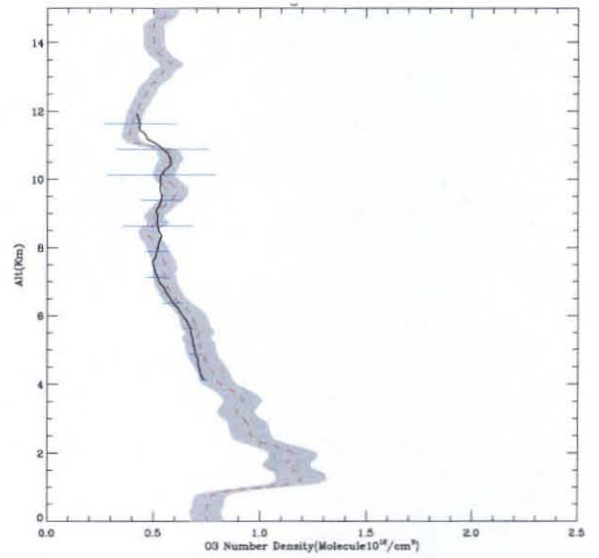
(a)   (b)

Fig. 10.   Continuous DIAL measurements compared with local ozonesonde measurement. (a

Coincident ozone DIAL retrievals (solid lines) with 750 m vertical resolution and 30 min

integration time and ozonesonde profile (dash line) with ±10% envelope on 12/23/06. The

ozonesonde measurement was made at 13:00 local time. (b) Average Dial profile of the 10

retrievals shown in (a) and its 1-sigma standard deviation.